crystals

MDPI

Article

$AgSn[Bi_{1-x}Sb_x]Se_3$: Synthesis, Structural Characterization, and Electrical Behavior

Paulina Valencia-Gálvez [1], Daniela Delgado [1], María Luisa López [2], Inmaculada Álvarez-Serrano [2], Silvana Moris [3,*] and Antonio Galdámez [1,*]

1 Departamento de Química, Facultad de Ciencias, Universidad de Chile, Las Palmeras 3425, Santiago 7800003, Chile; paulygav@uchile.cl (P.V.-G.); dani.delgado.m@gmail.com (D.D.)
2 Departamento de Química Inorgánica, Facultad de Ciencias Químicas, Universidad Complutense, 28040 Madrid, Spain; marisal@quim.ucm.es (M.L.L.); ias@quim.ucm.es (I.Á.-S.)
3 Centro de Investigación de Estudios Avanzados del Maule (CIEAM), Vicerrectoría de Investigación y Postgrado, Universidad Católica del Maule, Avenida San Miguel 3605, Talca 3480112, Chile
* Correspondence: smoris@ucm.cl (S.M.); agaldamez@uchile.cl (A.G.)

Abstract: Herein, we report the synthesis, characterization, and electrical properties of lead-free $AgSn_m[Bi_{1-x}Sb_x]Se_{2+m}$ (m = 1, 2) selenides. Powder X-ray diffraction patterns and Rietveld refinement data revealed that these selenides consisted of phases related to NaCl-type crystal structure. The microstructures and morphologies of the selenides were investigated by backscattered scanning electron microscopy, energy-dispersive X-ray spectroscopy, and high-resolution transmission electron microscopy. The studied $AgSn_m[Bi_{1-x}Sb_x]Se_{2+m}$ systems exhibited typical p-type semiconductor behavior with a carrier concentration of approximately ~$+10^{20}$ cm^{-3}. The electrical conductivity of $AgSn_m[Bi_{1-x}Sb_x]Se_{2+m}$ decreased from ~3.0 to ~10^{-3} $S{\cdot}cm^{-1}$ at room temperature (RT) with an increase in m from 1 to 2, and the Seebeck coefficient increased almost linearly with increasing temperature. Furthermore, the Seebeck coefficient of $AgSn[Bi_{1-x}Sb_x]Se_3$ increased from ~+36 to +50 $\mu V{\cdot}K^{-1}$ with increasing Sb content (x) at RT, while its average value determined for $AgSn_2[Bi_{1-x}Sb_x]Se_4$ was approximately ~+4.5 $\mu V{\cdot}K^{-1}$.

Keywords: selenides; seebeck coefficient; lead-free thermoelectric materials

Citation: Valencia-Gálvez, P.; Delgado, D.; López, M.L.; Álvarez-Serrano, I.; Moris, S.; Galdámez, A. $AgSn[Bi_{1-x}Sb_x]Se_3$: Synthesis, Structural Characterization, and Electrical Behavior. *Crystals* **2021**, *11*, 864. https://doi.org/10.3390/cryst11080864

Academic Editors: Michael Waltl and Dmitri Donetski

Received: 13 June 2021
Accepted: 23 July 2021
Published: 26 July 2021

1. Introduction

The multicomponent silver chalcogenide family $AgM^1M^2Q_3$ (M^1 = Pb, Sn; M^2 = Bi, Sb, and Q = S, Se, Te) contains several thermoelectric phases [1–7]. Kanatzidis et al. extensively investigated the properties of chalcogenide compounds, which represent promising thermoelectric materials [8–10]. In particular, $AgPb_mSbTe_{2+m}$, $Ag_{1.33}Pb_{1.33}Sb_{1.33}Te_4$, and $AgPb_{18}SbSe_{20}$ were examined in detail. $AgPb_mSbTe_{2+m}$ is a class of candidates for thermoelectric materials, which is often abbreviated as LAST (lead, antimony, silver, tellurium)-m. These compounds can be envisioned as an alloy between two cubic chalcogenides, PbTe- and $AgSbTe_2$: $(PbTe)_m$–$AgSbTe_2$. Electrical transport studies have shown that the thermoelectric properties of this system can be fine-tuned via compositional parameter m. Recently, Dutta et al. and Cai et al. reported the thermoelectric properties of n-type $AgPbBiSe_3$ and p-type $AgPb_mSbSe_{2+m}$ families [11,12]. These phases possess high Seebeck coefficients S equal to approximately −131 $\mu V{\cdot}K^{-1}$ ($AgPbBiSe_3$) and +130 $\mu V{\cdot}K^{-1}$ ($AgPb_mSbSe_{2+m}$; m = 10). In addition, $AgPbBiSe_3$ exhibits S values of −131 and –204 $\mu V{\cdot}K^{-1}$ at 296 and 770 K, respectively, and electrical conductivity σ of 63 $S{\cdot}cm^{-1}$ at room temperature (RT) and 72 $S{\cdot}cm^{-1}$ at 818 K. As expected, these values increased with an increase in the halogen doping concentration. Experimental single-crystal X-ray diffraction (XRD) and high-resolution transmission electron microscopy (HRTEM) studies revealed that the electrical properties of these chalcogenides were related to the presence of nanoscopic inhomogeneities [4,13,14]. Electron diffraction and energy-dispersive X-ray spectroscopy

(EDS) analyses demonstrated that Ag-Sb-rich nanostructures were embedded into the PbTe lattice of $(PbTe)_m$–$AgSbTe_2$ systems, whose electronic behaviors were sensitive to their microstructures.

Owing to the strict environmental regulations related to the use of lead-based materials, novel compounds, such as lead-free *p*-type $AgSnSbSe_3$, *n*-type BiAgSeS, *p*-type $(SnTe)_m$–$AgSbTe_2$, *p*-type $AgSn_mSbSe_2Te_m$, and $(SnTe)_m$–$AgBiTe_2$ systems, have been prepared recently [15–21]. $(SnTe)_m$–$AgBiTe_2$ systems could be viewed as alloys of two cubic chalcogenides, SnTe and $AgBiTe_2$. These chalcogenides possess low thermal conductivities and large positive Seebeck coefficients. The influence of chemical substitution on the thermoelectric properties of the listed chalcogenides has been discussed in several studies. For example, the chemical substitution of Se by Te in $AgSnSbSe_3$ (e.g., $AgSnSbSe_{1.5}Te_{1.5}$) results in the formation of a material with an average power factor $S^2 \cdot \sigma$ of ~9.54 $\mu W \cdot cm^{-1} \cdot K^{-2}$ (400–778 K) [15]. Herein, we report the synthesis, characterization, and electrical properties of novel lead-free $AgSn_m[Bi_{1-x}Sb_x]Se_{2+m}$ (m = 1 and 2) systems obtained via the isoelectronic substitution of Bi by Sb atoms. $AgSn_m[Bi_{1-x}Sb_x]Se_{2+m}$ compounds could be considered alloys of SnSe and $Ag(Bi_{1-x}Sb_x)Se_2$, corresponding to $(SnSe)_m$–$Ag(Bi_{1-x}Sb_x)Se_2$ systems. Tan et al. suggested that bismuth was a better neutralizer of positive holes in the SnTe structure than antimony [18]. In this study, we investigated the electrical and structural characteristics of selenides that were selected because bismuth was a more efficient electron donor than antimony. Powder X-ray diffraction patterns and Rietveld refinement results were consistent with phases related to the cubic NaCl-type lattice. The microstructures and morphologies of these systems were investigated using scanning electron microcopy (SEM) and high-resolution transmission electron microscopy (HRTEM).

2. Materials and Methods

Silver powder (99.99% purity, Sigma-Aldrich, St. Louis, MO, USA), antimony powder (99.99% purity, Sigma-Aldrich, St. Louis, MO, USA), tin powder (99.9% purity, Sigma-Aldrich, St. Louis, MO, USA), selenium powder (99.99% purity, Sigma-Aldrich, St. Louis, MO, USA), bismuth powder (99.99% purity, Merck, Kenilworth, NJ, USA), and sulfur powder (99.99% purity, Merck, Kenilworth, NJ, USA) were used in this study. All experiments were performed under a dry and oxygen-free argon atmosphere. Selenide phases with the nominal compositions were prepared via the solid-state reaction of Ag, Sn, Bi, Sb, and Se powders mixed in the stoichiometric proportions inside evacuated quartz ampoules. The reaction mixture was gradually heated to 1223 K at a rate of +50 K/h, maintained at this temperature for ~12 h, and slowly cooled to RT at 8 K/h. Chemical compositions of the samples were determined by scanning electron microscopy (SEM, JEOL 5400 system, Tokyo, Japan) and energy-dispersive X-ray spectroscopy (EDS, Oxford LinK ISIS microanalyzer, Oxford Instruments, Abingdon, UK). XRD patterns were obtained at RT using a Bruker D8 advanced powder diffractometer (Bruker, Billerica, MA, USA) with CuKα radiation over the 2θ range of 5–80° at a step size of 0.01°. In addition, XRD patterns were also collected at temperatures varying from RT to 77 K using a PANalytical X'Pert PROMPD diffractometer (CuKα1 = 1.544426 Å, CuKα2 = 1.54098 Å) over the 2θ range of 5–80° at a step size of 0.0167° (Malvern Panalytical, Boulder, CO, USA). The diffractometer was equipped with a heating chamber (Anton Paar HTK1200, PANanalytical BV, Boulder, CO, USA). The collected data were analyzed by two Rietveld refinement software programs: Fullprof and MAUD [22–24]. A standard LaB_6 sample was used to measure instrumental profiles. SEM–EDS and powder XRD analyses revealed that the $AgSn_m[Bi_{1-x}Sb_x]Se_{2+m}$ (m = 1 and 2) samples have been successfully prepared. On the other hand, reaction products with the nominal stoichiometry of $AgSn_m[Bi_{1-x}Sb_x]Se_{m+2}$ (m = 4, 8, 10, and 12) included 10–30% SnSe impurities. For example, the reaction products with the nominal compositions $AgSn_8[Bi_{0.8}Sb_{0.2}]Se_{10}$ and $AgSn_4[Bi_{0.2}Sb_{0.8}]Se_6$ contained $AgSnMSe_3$, SnSe, and some unidentified impurities. Differential thermal analysis (DTA) and thermogravimetric analysis (TGA) of the samples were performed using a Rheometric Scientific STA 1500H/625 thermal analysis system (Rheometric Scientific, Inc., Piscataway, NJ, USA).

To record DTA/TGA curves, the samples were heated from RT to 1273 K in an argon atmosphere or to 673 K in air at a rate of 10 K/min. A high-temperature melting method was applied to obtain suitable ingot samples for Seebeck measurements. The obtained reaction samples were crushed into powders and placed into a quartz ampoule, which was evacuated and flame-sealed under an argon atmosphere. This tube was then placed into a furnace at 1073 K for ~2 h and then slowly cooled to RT at 8 K/h. Subsequently, these ingots were cut and polished for measurements of their transport properties. Although various experimental conditions (temperature, cooling rate, melting, and cooling) were utilized, the ingots of some chemical compositions of $AgSn_2[Bi_{1-x}Sb_x]Se_4$ and $AgSn[Bi_{1-x}Sb_x]Se_3$ were too brittle and broken. In the case of the $AgSn_2[Bi_{1-x}Sb_x]Se_4$ composition, a visible change in the pellet appearance (the presence of small holes on the pellet surface) was observed in some samples during thermal cycling. Electrical conductivities of the samples were measured by a pellet method, in which pellets were uniaxially pressed at 5×10^8 Pa to form cylindrical specimens with diameters of ~7 mm and thicknesses of ~1–2 mm. The pelletized specimens were sintered at 673, 923, and 993 K for 12 and 24 h in an argon atmosphere (Ar 12 or 24 h) and in air at 673 K for 12 h (air 12 h). The low-temperature (20–300 K) Hall effect and Seebeck coefficient measurements were performed using a physical property measurement system (PPMS). High-temperature electrical conductivities were measured using an ECOPIA HMS 2000 system (ECOPIA, Anyang-city, Gyeonggi-do, South Korea) and Keithley 6220 current source/Keithley 2182A nanovoltmeter (Tektronix, Inc., Beaverton, OR, USA) with a four-probe contact geometry. High-temperature Seebeck coefficients were determined by a laboratory-made system. The densities of the ingot and pellet samples were computed from their dimensions and masses; the obtained magnitudes were equal to ~90–92% of the theoretical values.

3. Results and Discussion

3.1. Structures and Compositions of Selenide Samples

The backscattered electron images and EDS analyses of the powder samples, ingots, and pellets for electrical measurements revealed that the chemical compositions of all selenide samples were uniform throughout the scanned region (Figure 1). No secondary intergranular phases were observed in the $AgSn[Bi_{1-x}Sb_x]Se_3$ samples (x = 0, 0.2, 0.3, 0.8) within the detection limits of this technique. Figure 2 presents the PXRD patterns for the $AgSn_m[Bi_{1-x}Sb_x]Se_{2+m}$ samples with m = 1 and 2. Their sharpness indicates high crystallinity, and the observed interlayer spacing was in good agreement with the calculated interplanar spacing d. The SEM–EDS and XRD analyses suggest that the prepared materials could be regarded as a continuous solid solution between SnSe and $AgBiSe_2$, similarly to the SnTe–$NaSbTe_2$ and SnTe–$NaBiTe_2$ systems [25]. In the case of $AgSn_2[Bi_{1-x}Sb_x]Se_4$ samples (m = 2), the PXRD patterns show an extremely small amount of SnSe impurities.

A structural analysis of the $AgPb_mSbTe_{2+m}$ phases carried out by Quarez et al. by HRTEM analyses and single-crystal XRD demonstrated that the structure of these phases could be refined in the space group $Pm\bar{3}m$, as well as in a lower symmetric space group such as *P4/mmm* [13]. It is extremely complicated to choose the adequate symmetry since all refinements were acceptable due to the coherent X-ray scattering amplitudes, which are extremely similar, and the super-structure reflections in the powder pattern are especially hard to see.

The XRD patterns obtained for these phases were refined in *the Pm-3m* and *P4/mmm* space groups. In both space groups, the two sites at the (0,0,1/2) and (1/2,1/2,0) positions were fully occupied by Ag, Sb, Sn, or Bi atoms. The RT Rietveld refinement profiles of $AgSnBiSe_3$ based on the cubic and tetragonal models are shown in Figure 3. The following unit cell parameters were obtained: cubic unit cell a_c = 5.86180(6) Å, tetragonal ($a_t = b_t \approx a_c\sqrt{2}/2$, $c_t \approx a_c$) unit cell a_t = 4.14365 (16), and c_t = 5.8631(4) Å. The tetragonal model contained two cation sites (1b and 1c Wyckoff sites), which were fully occupied by the randomly distributed Ag, Sn, and Bi cations. Selenium atoms adopted close cubic packing at the 1a and 1d Wyckoff sites. Both structural models were consistent with the

experimental data as well as with the obtained R factors; therefore, we were unable to identify the best structural model for this material (Tables S1 and S2). Moreover, $AgBiSe_2$ and $Ag(Bi,Sb)Se_2$ phases show interesting structural transitions with both temperature and composition. Thus, at room temperature the Sb-free samples have a hexagonal symmetry within the space group $Pm\bar{3}1$. As the Sb content increases, these phases show a rhombohedral symmetry ($R\bar{3}m$) [26].

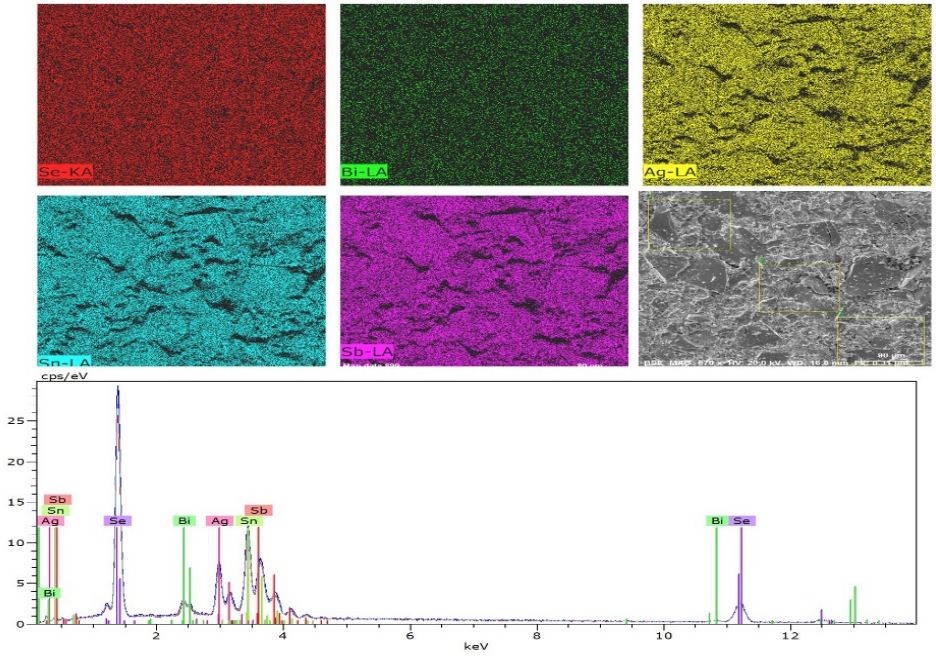

Figure 1. SEM analysis: representative EDS mapping images (powder sample) and backscattered electron image of $AgSn[Bi_{0.8}Sb_{0.2}]Se_3$ (20 kV, 670×).

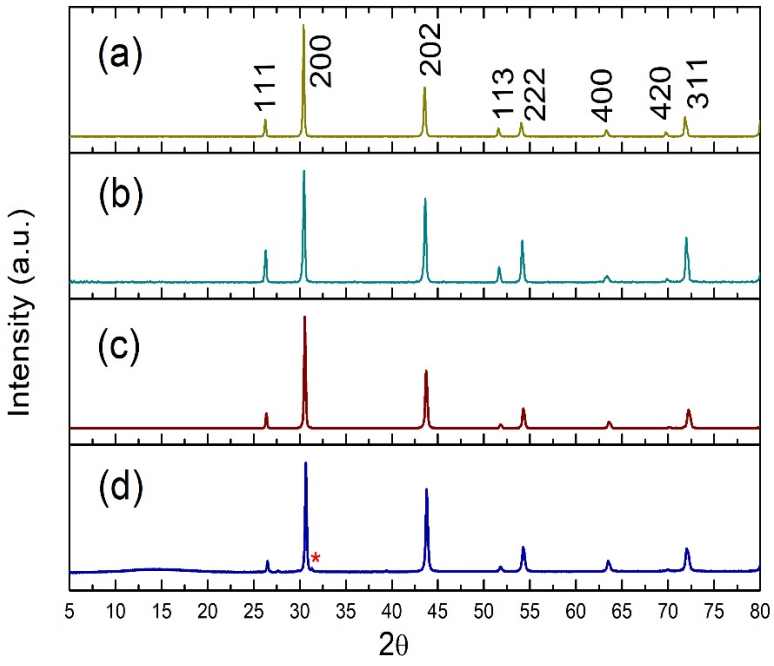

Figure 2. Representative powder XRD patterns at room temperature of: (**a**) $AgSnBiSe_3$ showing the corresponding *hkl* miller indices, (**b**) $AgSn[Bi_{0.8}Sb_{0.2}]Se_3$, (**c**) $AgSn[Bi_{0.2}Sb_{0.8}]Se_3$, and (**d**) $AgSn_2[Bi_{0.2}Sb_{0.8}]Se_4$ (the red asterisk indicates a secondary reflection indexed to the SnSe *Pnma* space group).

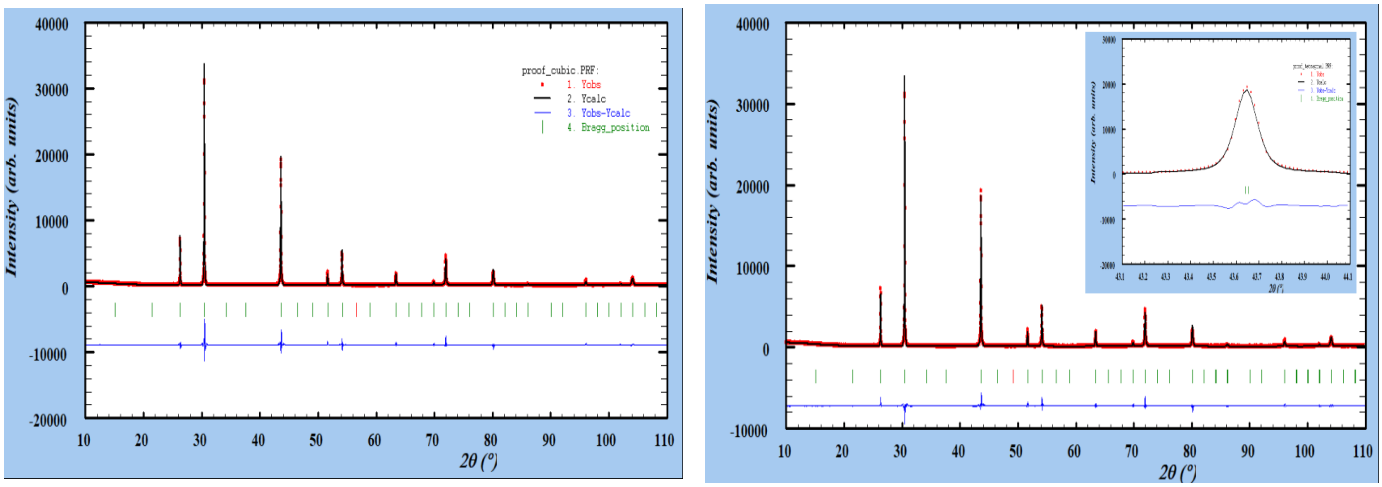

(**a**) (**b**)

Figure 3. Rietveld refinement of the XRD data obtained for $AgSnBiSe_3$ (including the profile fit, profile difference, and profile residuals), which was performed with the Fullprof software. (**a**) Cubic *Pm-3m* and (**b**) tetragonal *P4/mmm* space groups at RT (the insert shows a selected area). Bragg's R-factors of the cubic space group were *R*b = 3.32 and *R*wp = 4.44. Bragg's R-factors of the tetragonal space group were *R*b = 5.72 and *R*wp = 4.88.

XRD patterns of $AgSn[Bi_{1-x}Sb_x]Se_3$ and $AgSn_2[Bi_{1-x}Sb_x]Se_4$ were refined using the cubic and tetragonal models (Table S3 and Figure S1—see in Supplementary Materials). As expected, the cell volume increased slightly after replacing Bi atoms (radius: 1.63 Å) by Sb atoms (radius: 1.53 Å), and the resulting solid solutions did not obey Vegard's law.

In order to analyze the microstructural features of the samples, a study by HRTEM and electron diffraction was also carried out. Small crystals with octahedral $AgSnBiSe_3$ shapes were observed. The mean atomic compositions (determined from the EDS data) of the studied samples were similar to the expected compositions. Figure 4 displays the electron diffraction (ED) patterns obtained along [111]c zone axis for the different selected regions of the selenide samples. It shows that different contrast zones are predominant in the analyzed crystals, as shown in Figure 4.

The Miller indices are calculated considering a cubic symmetry in both models and they are indicated in the image. However, spots of weak intensity that are prohibited in the space group $Fm\bar{3}m$ are clearly observed. It is noteworthy that these weak spots indicate the appearance of different symmetries. The new Miller indices can be obtained from the Equations (1) and (2) where the unit cell transformation from cubic to tetragonal or hexagonal were considered.

Equation (1): cubic to tetragonal.

$$\begin{aligned} h_t &= \tfrac{1}{2}(h_c - k_c) \\ K_t &= \tfrac{1}{2}(h_c + k_c) \\ l_t &= l_c \end{aligned} \quad (1)$$

Equation (2): cubic to hexagonal

$$\begin{aligned} h_h &= \tfrac{1}{2}(-k_c + l_c) \\ K_h &= \tfrac{1}{2}(h_c - l_c) \\ l_h &= h_c + k_c + l_c \end{aligned} \quad (2)$$

Thus, in the micrograph of Figure 4a, these weak spots would not be compatible with a P-type cubic lattice, nor with a tetragonal symmetry, as shown in the diagrams below the ED images. However, they would be compatible with a hexagonal symmetry. On the contrary, only a $Pm\bar{3}m$ cubic space group seems to be consistent with the superstructure spots (Figure 4b). These results indicate that the $AgSnBiSe_3$ phase exhibits nanoscopic

inhomogeneities, in good agreement with those reported for similar phases [10,13,27]. In addition, nanoregions with different orientations or symmetries were detected (Figure 4c). This is consistent with the results reported previously [13].

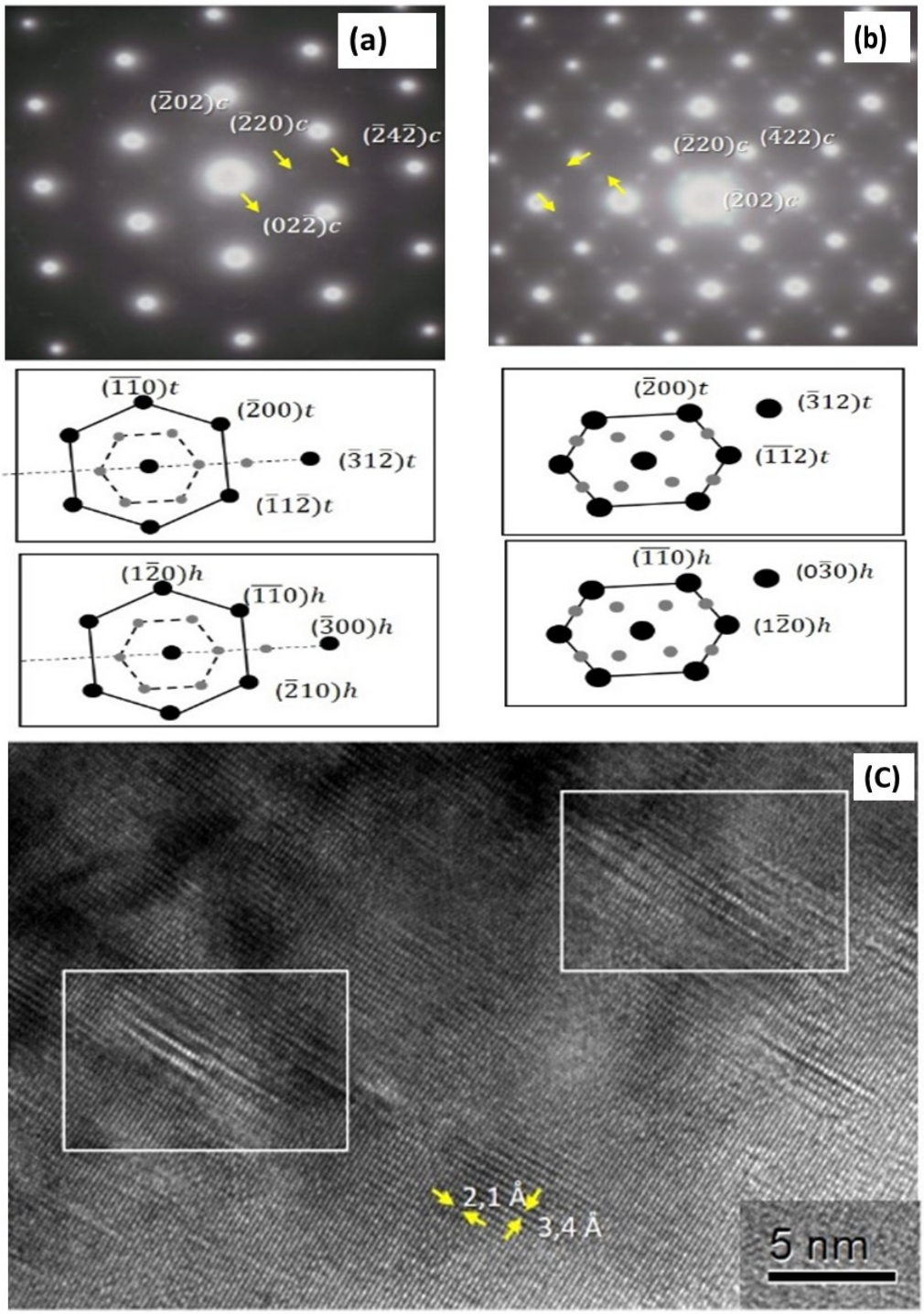

Figure 4. High-resolution transmission electron microscopy (HRTEM) study for $AgSnBiSe_3$, showing (**a**,**b**) ED patterns along [111]*c* zone axis and schemes for different symmetries (*h* and *t* refer to hexagonal and tetragonal, respectively), and (**c**) representative HRTEM image showing disorder regions apparent at the nanoscale.

3.2. Electrical Properties and Seebeck Coefficients

The melting point of the prepared selenide samples was ~1000 K, and the pellets were sintered at 673, 923, and 993 K (see the experimental details). In addition, TGA was conducted in air from RT to 673 K to produce stable thermal and gravimetric signals. The obtained TGA results were consistent with the SEM–EDS and powder XRD data (Figures S2 and S3). The $AgSn[Bi_{1-x}Sb_x]Se_3$ pellets exhibited a microstructure with particle sizes of ~2–14 μm and isolated regions with a grain size of ~20 μm. The XRD patterns of the selenide samples recorded at various temperatures between RT and 77 K exhibit high structural and thermal stabilities (Figure S4). Their XRD and backscattered SEM–EDX analyses were performed after electrical measurements.

Figure 5a shows the temperature dependence of the electrical conductivity σ of the $AgSnBiSe_3$ sample. For pristine $AgSnBiSe_3$, electrical conductivity increases with increasing temperature, indicating the phase exhibits semiconductor behavior. The σ was thermally activated at low temperatures. In addition, the σ of the samples sintered at 923 K in Ar for 48 h was ~2.1 $S{\cdot}cm^{-1}$ at 240 K. This value was approximately two times higher than the σ of the samples sintered at 673 K in Ar or air (~1.1 $S{\cdot}cm^{-1}$) at 240 K. The $AgSnBiSe_3$ sample with a cylindrical shape (ϕ~6.00 mm and s~1.0 mm) cut from the ingot of pristine material, exhibited an electrical conductivity of ~4.0 $S{\cdot}cm^{-1}$ at RT. The σ magnitudes obtained at 80 K and 140 K were equal to 0.24 and 0.75 $S{\cdot}cm^{-1}$, respectively. The electrical conductivity σ of $AgSn_m[Bi_{1-x}Sb_x]Se_{2+m}$ decreased from ~3.0 to 10^{-3} $S{\cdot}cm^{-1}$ at RT with an increase in m from 1 to 2 (Table 1). These values are comparable to those of $AgSn_mSbSe_{m+2}$ (~10^{-3} − 93 $S{\cdot}cm^{-1}$ for m = 1–12) [15].

Table 1. Electrical conductivity (σ) and Seebeck coefficient of $AgSn[Bi_{1-x}Sb_x]Se_3$ and $AgSn_2[Bi_{1-x}Sb_x]Se_4$.

	σ at RT ($S{\cdot}cm^{-1}$) £	**Seebeck Coefficient at RT ($\mu V{\cdot}K^{-1}$) §**	**Seebeck Coefficient at 450 K ($\mu V{\cdot}K^{-1}$) § ***
$AgSnBiSe_3$	2.46	+7.39	+89.6
$AgSnBi_{0.8}Sb_{0.2}Se_3$	3.22	+36.2	-
$AgSnBi_{0.2}Sb_{0.8}Se_3$	2.97	+49.8	-
$AgSn_2Bi_{0.8}Sb_{0.2}Se_4$	1.22×10^{-3}	+3.93	+92.0
$AgSn_2Bi_{0.2}Sb_{0.8}Se_4$	2.35×10^{-3}	+4.91	+114.1

£ pelletized specimens and § ingot samples. * Because of the brittleness and chemical unstable nature of some samples, the Seebeck coefficients at 450 K were not reported in this table (see details in materials and methods section). The densifications magnitudes were equal to ~90–92%.

The low-temperature $\sigma(T)$ of $AgSnBiSe_3$ followed a standard variable range hopping (VRH) model described by the following equation:

$$\sigma = \sigma_0 \, exp\left[-\left(\frac{T_0}{T}\right)^{1/4}\right] \quad (3)$$

where σ_0 is the residual conductivity, and T_o is the characteristic temperature. To validate the VRH model, we fitted the experimental data with Equation (3). The obtained results presented in the inset of Figure 5a indicate that the transport mechanism regime involved the VRH process. The plot of ln σ versus $T^{-1/4}$ changed its the slope at around ~160 K. The occurrence of the hopping process depends on the energy difference and relationship between the Fermi level and the mobility edge. This behavior was previously observed at low temperatures for other selenides, such as Pb-doped Cu_2SnSe_3 and $Cu_yFe_4Sn_{12}X_{32}$ spinels [28,29].

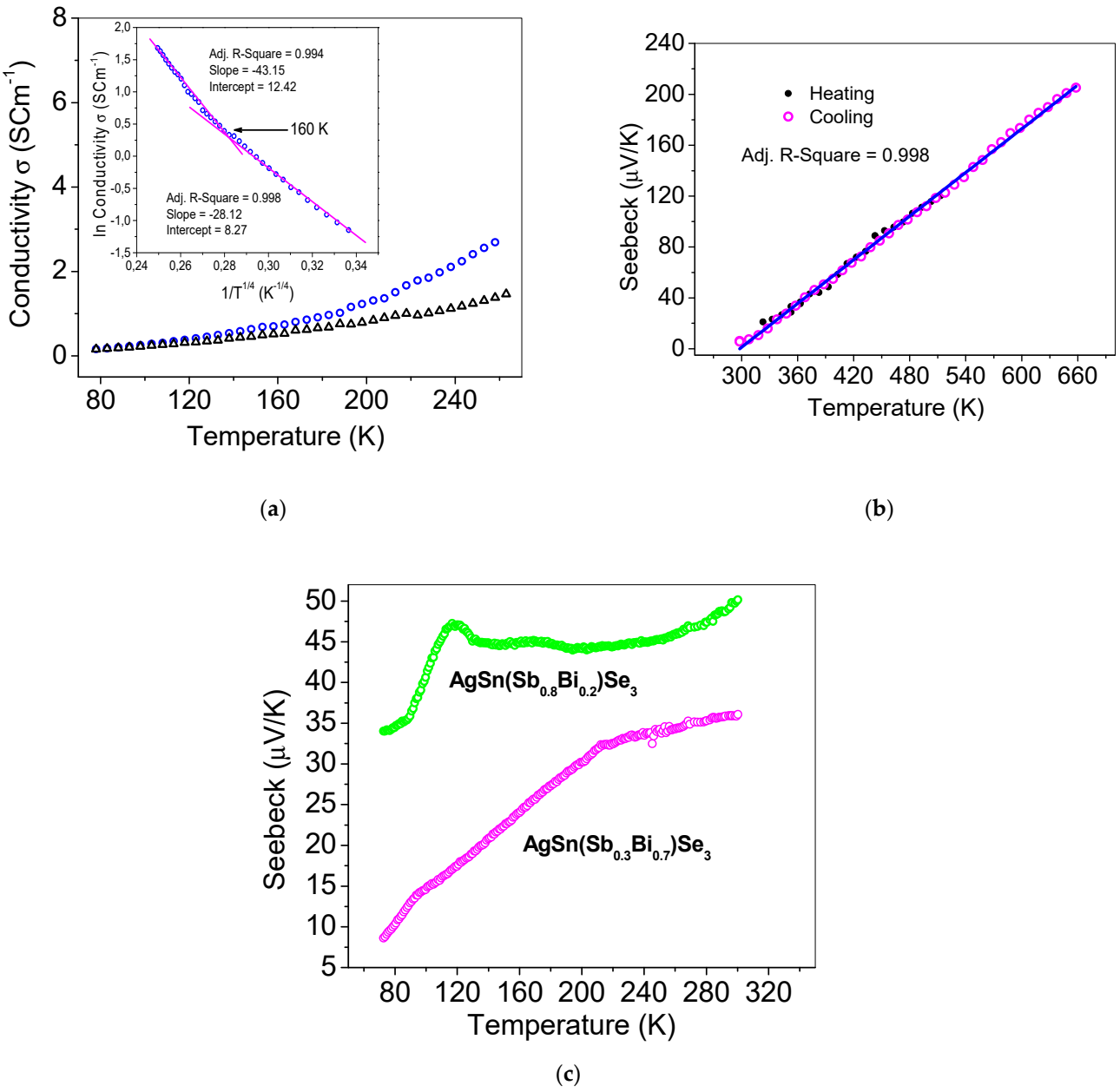

Figure 5. Temperature dependences of the electrical conductivity and Seebeck coefficient determined for AgSn[$Bi_{1-x}Sb_x$]Se_3. (**a**) Electrical conductivity–temperature plots of $AgSnBiSe_3$ sintered at 673 K in Ar 12 h (open triangles) and $AgSnBiSe_3$ sintered at 923 K in Ar for 48 h (open circles). The inset shows the ln σ vs. $T^{-1/4}$ curve, and the solid lines denote the linear fit of the experimental data. (**b**) Plots of Seebeck coefficient vs. temperature (heating–cooling cycle measurements) obtained for $AgSnBiSe_3$. (**c**) Plots of Seebeck coefficient vs. temperature obtained for AgSn[$Bi_{1-x}Sb_x$]Se_3 (x = 0.8 and 0.3) in the low-temperature range.

The positive Seebeck coefficient values of the $AgSn_m[Bi_{1-x}Sb_x]Se_{2+m}$ systems (m = 1 and 2) obtained via the isoelectronic substitution of a fraction of Bi atoms with Sb indicates that holes are the dominant conduction carriers (Table 1). The temperature dependences of the Seebeck coefficient of AgSn[$Bi_{1-x}Sb_x$]Se_3 in the high-temperature and low-temperature ranges are shown in Figure 5b,c, respectively. The Seebeck coefficient of AgSn[$Bi_{1-x}Sb_x$]Se_3 (m = 1) selenides increased from ~+36 μV·K^{-1} (x = 0.2) to +50 μV·K^{-1} (x = 0.8) with increasing Sb content at RT. This value is approximately four times lower than that of $AgSnSbSe_3$ (+179 μV·K^{-1}) and is comparable with the Seebeck coefficient of SnTe at 300 K (+40 μV K^{-1}). Consequently, the power factor ($S^2 \cdot \sigma$) of $AgSnBiSe_3$ was ~0.1 μW·cm^{-1}·K^{-2}. Power factors of 5–12 μW·cm^{-1}·K^{-2} were obtained for $AgSn_mSbTe_{m+2}$ systems at 300 K [21]. The S

values of $AgSn_2[Bi_{1-x}Sb_x]Se_4$ selenides increased from ~+3.9 (x = 0.2) to ~+4.9 $\mu V \cdot K^{-1}$ (x = 0.8) with an increase in the Sb content at RT (Table 1). The average Seebeck coefficient of the $AgSn_2[Bi_{1-x}Sb_x]Se_4$ samples was ~+4.5 $\mu V \cdot K^{-1}$. This value is approximately ten times lower than that determined for $AgSn[Bi_{0.2}Sb_{0.8}]Se_3$ (~+50 $\mu V \cdot K^{-1}$). Kanatzidis et al. reported that the Seebeck coefficients of p-type $AgSn_mSbSe_{2+m}$ systems decreased from ~+179 to 51 $\mu V \cdot K^{-1}$ with an increase in m from 1 to 12 at RT [15]. The $AgSn_2[Bi_{1-x}Sb_x]Se_4$ selenide samples exhibited S values of ~+92 $\mu V \cdot K^{-1}$ (x = 0.2) and +114 $\mu V \cdot K^{-1}$ (x = 0.8) at 450 K. The temperature dependence of S obtained for $AgSn_2[Bi_{1-x}Sb_x]Se_4$ indicate degenerate semiconductor properties and is consistent with the behavior previously reported for $AgSn_{10}SbSe_2Te_{10}$ [17].

The temperature dependence of the Seebeck coefficient of degenerate semiconductors is expressed by the formula

$$S = \left[\frac{8\pi^{2/3}k_B^2(r+3/2)}{3^{5/3}eh^2}\right]\left(\frac{m^*}{n^{2/3}}\right)T \quad (4)$$

where S is the Seebeck coefficient, m^* is the effective mass, k_B is Boltzmann's constant, e is the charge of an electron, h is Planck's constant, and n is the carrier concentration [17]. In this study, the Seebeck coefficient was fitted in the temperature range of 300 K $\leq$ T $\leq$ 700 K to determine the density-of-states effective mass (m^*). Figure 5b shows the plot of Seebeck coefficient vs. temperature constructed for $AgSnBiSe_3$ in the temperature range from RT to 670 K. The results of Hall measurements revealed that the carrier concentration in the selenide samples was approximately ~+10^{20} cm^{-3} at high temperatures. The results of Seebeck measurements conducted for $AgSnBiSe_3$ implied a large m^*~7·m_0 with an acoustic phonon scattering mechanism ($r = -1/2$) and m^*~3·m_0 with an ionized impurity scattering mechanism ($r = 3/2$). Large density-of-states effective mass, m^*~4.7−1.6·m_0 and m^*~6·m_0, were obtained for $AgSn_{10}SbSe_2Te_{10}$ and $Ag_{0.85}SnSb_{1.15}Te_3$, respectively [17,30] In addition, large values of m^* are usually obtained by the single parabolic band (SPB) model in degenerate samples. However, measurements of carrier concentration and mobilities at low temperature would be required to support this model.

4. Conclusions

SEM–EDS and powder XRD analyses revealed that the $AgSn_m[Bi_{1-x}Sb_x]Se_{2+m}$ (m = 1 and 2) samples have been successfully prepared at high temperatures via solid-state reactions. The HRTEM and XRD analysis of $AgSnBiSe_3$ indicated the presence of nanoregions with different symmetries, in good agreement with that reported for similar phases. The electrical conductivity of p-type $AgSn_m[Bi_{1-x}Sb_x]Se_{2+m}$ semiconductor decreased with an increase in m from 1 to 2. The linear plot of ln σ vs. $T^{-1/4}$ obtained for $AgSnBiSe_3$ indicated that the transport mechanism in the low-temperature regime included the VRH process. The positive Seebeck coefficients of the suggested that holes were the dominant conduction carriers. The Seebeck coefficient of $AgSn[Bi_{1-x}Sb_x]Se_3$ (m = 1) selenides increased from ~+36 (x = 0.2) to ~+50 $\mu V \cdot K^{-1}$ (x = 0.8) at RT with an increase in x.

Supplementary Materials: The following materials are available online at https://www.mdpi.com/article/10.3390/cryst11080864/s1. Table S1 and S2: Final atomic parameters determined through Rietveld refinement using the Fullprof program; Figure S1: Powder XRD data obtained for the $AgSn_m[Bi_{1-x}Sb_x]Se_{m+2}$ samples from the corresponding Rietveld refinement data; Table S3: Cell parameters of $AgSn[Bi_{1-x}Sb_x]Se_3$ and $AgSn_2[Bi_{1-x}Sb_x]Se_4$; Figure S2: SEM–BS images and ED spectrum of $AgSnBiSe_3$; Figure S3: XRD patterns of the sintered samples; Figure S4: Representative XRD patterns of the samples obtained upon heating/cooling from RT (bottom) to 77 K.

Author Contributions: Conceptualization, A.G. and S.M.; methodology and experiments, M.L.L., I.Á.-S., A.G., and D.D.; writing—original draft preparation, S.M., P.V.-G., M.L.L., I.Á.-S., and A.G.; electrical measurements, M.L.L. and P.V.-G. All authors have read and agreed to the published version of the manuscript.

Funding: This research received no external funding.

Acknowledgments: This work was supported by Fondecyt No. 1190856. The authors also acknowledge the CAI center of UCM (HRTEM). We would like to thank Daniela Ruiz and Daniela Herrera for their invaluable contributions to the synthesis of the samples and discussion of the experimental results.

Conflicts of Interest: The authors declare no conflict of interest.

References

1. Zeier, W.G.; Zevalkink, A.; Gibbs, Z.; Hautier, G.; Kanatzidis, M.; Snyder, J. Thinking Like a Chemist: Intuition in Thermoelectric Materials. *Angew. Chem. Int. Ed.* **2016**, *55*, 6826–6841. [CrossRef]
2. Zhang, X.; Zhao, L.-D. Thermoelectric materials: Energy conversion between heat and electricity. *J. Mater.* **2015**, *1*, 92–105. [CrossRef]
3. Minnich, A.J.; Dresselhaus, M.S.; Ren, Z.F.; Chen, G. Bulk nanostructured thermoelectric materials: Current research and future prospects. *Energy Environ. Sci.* **2009**, *2*, 466–479. [CrossRef]
4. Vineis, C.H.; Shakouri, A.; Majumdar, A.; Kanatzidis, M. Nanostructured Thermoelectrics: Big Efficiency Gains from Small Features. *Adv. Mater.* **2010**, *22*, 3970–3980. [CrossRef] [PubMed]
5. Hsu, K.F.; Loo, S.; Guo, F.; Chen, W.; Dyck, J.S.; Uher, C.; Hogan, T.; Polychroniadis, E.K.; Kanatzidis, M.G. Cubic $AgPb_mSbTe_{2+m}$: Bulk thermoelectric materials with high figure of merit. *Science* **2004**, *303*, 818–821. [CrossRef] [PubMed]
6. Pan, L.; Mitra, S.; Zhao, L.-D.; Shen, Y.; Wang, Y.; Felser, C.; Berardan, D. The Role of Ionized Impurity Scattering on the Thermoelectric Performances of Rock Salt $AgPb_mSnSe_{2+m}$. *Adv. Funct. Mater.* **2016**, *26*, 5149–5157. [CrossRef]
7. Xiao, Y.; Chang, C.H.; Zhang, X.; Pei, Y.; Li, F.; Yuan, B.; Gong, S.H.; Zhao, L.-D. Thermoelectric transport properties of $Ag_mPb_{100}Bi_mSe_{100+2m}$ system. *J. Mater. Sci. Mater. Electron.* **2016**, *27*, 2712–2717. [CrossRef]
8. Sootsman, J.; Chung, D.Y.; Kanatzidis, M. New and old concepts in thermoelectric materials. *Angew. Chem. Int. Ed.* **2009**, *48*, 8616–8639. [CrossRef] [PubMed]
9. Kanatzidis, M. Nanostructured thermoelectrics: The new paradigm? *Chem. Mater.* **2010**, *22*, 648–659. [CrossRef]
10. Slade, T.J.; Grovogui, J.; Kuo, J.; Anand, S.; Bailey, T.; Wood, M.; Uher, C.; Snyder, J.; Dravid, V.; Kanatzidis, M. Understanding the thermally activated charge transport in $NaPb_mSbQ_{m+2}$ (Q= S, Se, Te) thermoelectrics: Weak dielectric screening leads to grain boundary dominated charge carrier scattering. *Energy Environ. Sci.* **2020**, *13*, 1509–1518. [CrossRef]
11. Dutta, M.; Pal, K.; Waghmare, U.V.; Biswas, K. Bonding heterogeneity and lone pair induced anharmonicity resulted in ultralow thermal conductivity and promising thermoelectric properties in n-type $AgPbBiSe_3$. *Chem. Sci.* **2019**, *10*, 4905–4913. [CrossRef]
12. Cai, K.F.; He, X.R.; Avdeev, M.; Yu, D.H.; Cui, J.L.; Li, H. Preparation and thermoelectric properties of $AgPb_mSbSe_{m+2}$ materials. *J. Solid State Chem.* **2008**, *181*, 1434–1438. [CrossRef]
13. Quarez, E.; Hsu, K.-F.; Pcionek, R.; Frangis, N.; Polychroniadis, E.K.; Kanatzidis, M. Nanostructuring, compositional fluctuations, and atomic ordering in the thermoelectric materials $AgPb_mSbTe_{2+m}$. The myth of solid solutions. *J. Am. Chem. Soc.* **2005**, *127*, 9177–9190. [CrossRef] [PubMed]
14. Lioutas, C.H.; Frangis, N.; Todorov, I.; Chung, D.; Kanatzidis, M. Understanding nanostructures in thermoelectric materials: An electron microscopy study of $AgPb_{18}SbSe_{20}$ crystals. *Chem. Mater.* **2010**, *22*, 5630–5635. [CrossRef]
15. Luo, Y.; Hao, S.; Cai, S.; Slade, T.J.; Luo, Z.Z.; Dravid, V.P.; Yan, Q.; Kanatzidis, M.G. High Thermoelectric Performance in the New Cubic Semiconductor $AgSnSbSe_3$ by High-Entropy Engineering. *J. Am. Chem. Soc.* **2020**, *142*, 15187–15198. [CrossRef]
16. Pei, Y.L.; Wu, H.; Sui, J.; Li, J.; Berardan, D.; Barreteau, C.; Pan, L.; Dragoe, N.; Liu, W.S.; He, J.; et al. High thermoelectric performance in n-type BiAgSeS due to intrinsically low thermal conductivity. *Energy Environ. Sci.* **2013**, *6*, 1750–1755. [CrossRef]
17. Figueroa-Millon, S.; Álvarez-Serrano, I.; Bérardan, D.; Galdámez, A. Synthesis and transport properties of p-type lead-free $AgSn_mSbSe_2Te_m$ thermoelectric systems. *Mater. Chem. Phys.* **2018**, *211*, 321–328. [CrossRef]
18. Tan, G.; Shi, F.; Sun, H.; Zhao, L.D.; Uher, C.; Dravid, V.P.; Kanatzidis, M.G. SnTe–$AgBiTe_2$ as an efficient thermoelectric material with low thermal conductivity. *J. Mater. Chem. A* **2014**, *2*, 20849–20854. [CrossRef]
19. Falkenbach, O.; Schmitz, A.; Dankwort, T.; Koch, G.; Kienle, L.; Mueller, E.; Schlecht, S. Tin Telluride-Based Nanocomposites of the Type $AgSn_mBiTe_{2+m}$ (BTST-m) as Effective Lead-Free Thermoelectric Materials. *Chem. Mater.* **2015**, *27*, 7296–7305. [CrossRef]
20. Xing, Z.B.; Li, Z.Y.; Tan, Q.; Wei, T.R.; Wu, C.F.; Li, J.F. Composition optimization of p-type $AgSn_mSbTe_{m+2}$ thermoelectric materials synthesized by mechanical alloying and spark plasma sintering. *J. Alloys Compd.* **2014**, *615*, 451–455. [CrossRef]
21. Han, M.K.; Androulakis, J.; Kim, S.J.; Kanatzidis, M.G. Lead-Free Thermoelectrics: High Figure of Merit in p-type $AgSn_mSbTe_{m+2}$. *Adv. Energy Mater.* **2012**, *2*, 157–161. [CrossRef]
22. Rodriguez-Carvajal, J. Recent Advances in Magnetic Structure Determination by Neutron Powder Diffraction. *Phys. B* **1993**, *192*, 55–69. [CrossRef]
23. Rietveld, H.M. A Profile Refinement Method for Nuclear and Magnetic Structures. *J. Appl. Cryst.* **1969**, *2*, 65–71. [CrossRef]
24. Lutterotti, L. Total Pattern Fitting for the Combined Size–Strain–Stress–Texture Determination in Thin Film Diffraction. *Nucl. Inst. Methods Phys. Res. B* **2010**, *268*, 334–340. [CrossRef]

25. Slade, T.J.; Pal, K.; Grovogui, J.A.; Bailey, T.P.; Male, J.; Khoury, J.F.; Zhou, X.; Chung, D.Y.; Snyder, J.; Uher, C.; et al. Contrasting SnTe–$NaSbTe_2$ and SnTe–$NaBiTe_2$ Thermoelectric Alloys: High Performance Facilitated by Increased Cation Vacancies and Lattice Softening. *J. Am. Chem. Soc.* **2020**, *142*, 12524–12535. [CrossRef] [PubMed]
26. Sudo, K.; Goto, Y.; Sogabe, R.; Hoshi, K.; Miura, A.; Moriyoshi, C.; Kuroiwa, Y.; Mizuguchi, Y. Doping-Induced Polymorph and Carrier Polarity Changes in Thermoelectric Ag(Bi,Sb)Se_2 Solid Solution. *Inorg. Chem.* **2019**, *58*, 7628–7633. [CrossRef]
27. Bilc, D.; Mahanti, S.D.; Quarez, E.; Hsu, K.F.; Pcionek, R.; Kanatzidis, M.G. Resonant States in the Electronic Structure of the High Performance Thermoelectrics $AgPb_mSbTe_{2+m}$: The Role of Ag-Sb Microstructures. *Phys. Rev. Lett.* **2004**, *93*, 146403. [CrossRef] [PubMed]
28. Prasad, S.; Rao, A.; Gahtori, B.; Bathula, S.; Dhar, A.; Chang, C.C.; Kuo, Y.K. Low-temperature thermoelectric properties of Pb doped Cu_2SnSe_3. *Phys. B Condens. Matter* **2017**, *520*, 7–12. [CrossRef]
29. Suekuni, K.; Tsuruta, K.; Ariga, T.; Koyano, M. Variable-range-hopping conduction and low thermal conductivity in chalcogenide spinel $Cu_yFe_4Sn_{12}X_{32}$ (X = S, Se). *J. Appl. Phys.* **2011**, *109*, 083709. [CrossRef]
30. Androulakis, J.; Do, J.-H.; Pcionek, R.; Kong, H.; D'Angelo, J.J.; Hogan, T.; Quarez, E.; Palchik, O.; Uher, C.; Short, J.; et al. Coexistence of Large Thermopower and Degenerate Doping in the Nanostructured Material $Ag_{0.85}SnSb_{1.15}Te_3$. *Chem. Mater.* **2006**, *18*, 4719–4721. [CrossRef]